

Algorithm for subcycle terahertz scanning tunneling spectroscopy

S. E. Ammerman ^{*}, Y. Wei , N. Everett, V. Jelic , and T. L. Cocker [†]

Department of Physics and Astronomy, Michigan State University, East Lansing, Michigan 48824, USA

 (Received 31 August 2021; revised 1 February 2022; accepted 14 February 2022; published 24 March 2022)

Terahertz scanning tunneling microscopy (THz-STM) enables ultrafast measurements of surfaces, single molecules, and nanostructures with simultaneous subpicosecond temporal resolution and atomic spatial resolution. In pump-probe THz-STM experiments employing femtosecond optical pump pulses, lightwave-driven tunneling by a time-delayed THz probe pulse accesses the evolving differential conductance of the tunnel junction following photoexcitation. However, a general theoretical approach to extract the time- and voltage-dependent differential conductance from THz-STM measurements is lacking. Here, we introduce an algorithm for pump-probe THz scanning tunneling spectroscopy (THz-STS) analysis. Our approach allows us to reliably reconstruct the tunnel junction's differential conductance in steady-state or time-dependent scenarios from simulated THz-STS data. The algorithm achieves subcycle time resolution, which we demonstrate by retrieving dynamics faster than the bandwidth of the input THz voltage transient. Subcycle THz-STS will make lightwave-driven microscopy yet more powerful as a tool for characterizing ångström-scale ultrafast dynamics in novel materials.

DOI: [10.1103/PhysRevB.105.115427](https://doi.org/10.1103/PhysRevB.105.115427)

I. INTRODUCTION

In terahertz scanning tunneling microscopy (THz-STM), a free-space THz pulse is coupled to the tip of a scanning tunneling microscope [1–20]. The near field of the THz pulse at the tip apex applies an ultrafast transient bias voltage to the current-voltage (I - V) characteristic of the tunnel junction, inducing an ultrafast current pulse. Nonlinearities in the I - V characteristic lead to a rectified component in the current pulse that can be measured by time-integrating electronics.

Ultrafast THz-STM experiments have employed a number of different pump-probe configurations to explore the dynamics of surfaces [6,7,9,14,16], single molecules [5,11,13], and nanostructures [4,14] with high spatiotemporal resolution. One of the primary pump-probe schemes involves photoexciting the tip-sample junction globally through the absorption of a femtosecond optical pump pulse, thereby stimulating a change to the tunneling conductance that decays back to the unexcited state over femtosecond to picosecond timescales. This evolution is imprinted on the rectified current generated by the time-delayed THz probe pulse. However, the interpretation of THz-STM measurements can be difficult, presenting a significant challenge to the prospect of pump-probe THz scanning tunneling spectroscopy (THz-STS).

The investigative power of steady-state STM is greatly enhanced by STS, which extracts rich spectroscopic information on the atomic scale [21,22]. STS measurements of the differential conductance (dI/dV) are approximately proportional to the local density of states (LDOS) of the sample [23–27]. In STS, a dI/dV spectrum is acquired by sweeping the static DC

bias and simultaneously applying a small-amplitude voltage modulation. The resulting current modulation is read out via lock-in detection to reveal the slope of the I - V characteristic as a function of voltage.

In contrast, in THz-STM, the voltage modulation is nine orders of magnitude faster and only a single oscillation cycle long. To compensate, the peak voltage of each THz transient is typically tuned to the volt scale. Since the THz voltage transient is created by a free-space electromagnetic pulse, it is also bipolar and is assumed to have a vanishing temporal integral. It accesses sample LDOS both above and below the Fermi level, such that the resulting current transient may also be bipolar. Regardless, the current-pulse bandwidth far exceeds that of the STM electronics, so its oscillatory details cannot be captured directly by the experimental modes demonstrated so far. Instead, THz-STM measurements detect the average rectified charge per THz pulse, Q_{THz} , as a shift in the DC current, $I_{\text{THz}} = fQ_{\text{THz}} = efN_e$, where f is the pulse repetition rate, e is the electric charge and N_e is the average number of rectified elementary charges per THz pulse.

In optical-pump/THz-STM-probe experiments, photoexcitation acts on material parameters such as the LDOS or the distribution of electrons within the LDOS, changing the junction's differential conductance, and hence the Q_{THz} produced by a time-delayed THz probe pulse. Notably, the photoexcited state decays back to the ground state along the same time axis as the oscillations of the THz voltage. Therefore, the THz voltage transient not only sweeps between positive and negative bias up to a selected peak voltage, but also samples an evolving I - V characteristic, making the rectified charge a convolution over both voltage and time that must be disentangled. The prospect of pump-probe THz-STS experiments that reveal complex material properties with simultaneous atomic spatial resolution and subcycle temporal resolution thus relies

^{*}ammerma9@msu.edu

[†]cockerty@msu.edu

on the development of an analytical framework capable of extracting the time-dependent differential conductance from THz-driven tunneling measurements.

Here, we present a THz-STs algorithm for recovering the differential conductance in steady-state or pump-probe experiments with sub-THz-cycle (i.e., subcycle) temporal resolution. Our algorithm requires as input only the THz voltage waveform and Q_{THz} as a function of peak THz voltage and pump-probe delay, i.e., no *a priori* knowledge of the sample LDOS is needed. The paper is structured as follows. In Sec. II, we present the model for THz-induced tunneling and rectification that is used to simulate THz-STs data based on a chosen I - V characteristic and THz voltage waveform. In Sec. III, we show that modeling the steady-state I - V characteristic as a power series allows us to determine the differential conductance from a polynomial fit to the rectified charge. The efficacy of this algorithm is demonstrated for some examples, each of which corresponds to a model physical system. In Sec. IV, we extend the algorithm to pump-probe THz-STs: We describe the time-dependent I - V characteristic as a power series in which each coefficient is time dependent, allowing us to deconvolve the decay of the differential conductance from the THz voltage waveform using the cross-correlation theorem. We further define the time resolution of pump-probe THz-STs and explore the possibility of extracting sample dynamics that are faster than the bandwidth of the THz probe pulse. Finally, in Sec. V, we discuss the limitations of the algorithm, the physics that may be investigated, and potential experiments.

II. ULTRAFast CHARGE RECTIFICATION

In THz-STM, the ultrafast voltage transient is supplied by a free-space electromagnetic pulse that is focused onto the STM tip apex. The peak electric field of the incoupled pulse can be varied without affecting the shape of the electric field waveform, e.g., using a pair of wire-grid polarizers. This electric field waveform, which can be detected by electro-optic sampling, is related to the THz voltage waveform applied to the tunnel junction by the transfer function of the tip-sample system. The transfer function depends on the incoupling geometry, the macroscopic, mesoscopic, and microscopic shape of the tip, the dielectric function of the tip material, and the spectral content of the pulse [7–10,13,16]. To address the uncertainty introduced by calculating (or simulating) the transfer function, *in situ* experimental approaches have been developed to measure the THz near-field at the tip apex [9,10,13,28]. In the following, we assume that the relevant THz voltage waveform can be measured directly by such an experiment. We therefore leave aside further discussion of the transfer function and base our simulation of ultrafast charge rectification (and subsequent inversion algorithm; see Sec. III onward) on a model THz voltage waveform given by

$$V_{\text{THz}}(t) = V_{\text{pk}} V_0(t), \quad (1)$$

where $V_0(t)$ is a normalized function describing the temporal structure of the waveform and V_{pk} is a scaling factor that corresponds to the peak voltage of $V_{\text{THz}}(t)$. An implicit assumption of this parametrization is that V_{pk} can be tuned without affecting $V_0(t)$, such that the transfer function does

not depend on the input THz field strength. It is also experimentally straightforward to invert the sign of the incoupled THz field, for example, by adding or subtracting a reflection from the THz beampath or inverting the bias in the case of a photoswitch source, so V_{pk} can be made positive or negative in our simulation.

It is also experimentally feasible to tune the incident electric field waveform, and hence $V_0(t)$. Carrier-envelope-phase (ϕ_{CEP}) control has been demonstrated for THz-induced tunneling [6–8], while arbitrary THz waveform shaping has been established [29] and may be combined with THz-STM in the future. However, the THz-STs algorithm outlined in the present paper is based on a constant (and arbitrary) $V_0(t)$ waveform shape. We believe this approach is the most experimentally accessible. Future THz-STs algorithms may utilize waveform control for further refinement.

It is important to note that, unlike for STM-coupled pulses at near-infrared frequencies [30], the field of a THz-coupled pulse can be treated (to a good approximation) as a purely quasistatic bias voltage applied across the STM junction. To illustrate why this is the case, we consider the Keldysh parameter [31,32], $\gamma = \omega\sqrt{2m_e}\Phi/(eE)$, where ω is the angular oscillation frequency of the electric field across the junction, m_e is the mass of the electron, Φ is the ionization energy or barrier height, e is the elementary charge, and E is electric field strength. The Keldysh parameter distinguishes between the multiphoton regime of optical nonlinearity ($\gamma > 1$) and the nonperturbative, strong-field regime ($\gamma < 1$), where field-driven tunneling dominates. For typical STM parameters and THz frequencies, $\gamma \sim 10^{-3}$, i.e., $\gamma \ll 1$.

Extending this concept, we can calculate the minimum voltage, V_{min} , that can be applied at a given frequency across a junction with tip-sample distance, d , while remaining in the strong-field regime [2], $V_{\text{min}}(\omega, d) = \omega d\sqrt{2m_e}\Phi/e$. In other words, the concept of lightwave-driven tunneling applies only for $V > V_{\text{min}}(\omega, d)$, and tunneling at lower voltages should be described by either a multiphoton process or a more complex treatment (near the crossover region). For a frequency of 1 THz and a typical STM tip height of 1 nm, V_{min} is on the order of a few mV, so experimentally relevant THz voltages behave as quasiinstantaneous, adiabatic voltage transients. Conversely, V_{min} increases linearly with frequency, such that it exceeds Φ/e for visible frequencies, meaning the lightwave-driven description is appropriate only in the case of field emission. Interestingly, this suggests that THz-driven tunneling uniquely spans mV to V voltage scales as a strong-field process while simultaneously maintaining subpicosecond temporal resolution.

In the THz-STM simulations presented here, the THz voltage transient defined in Eq. (1) acts on the tunnel junction I - V characteristic as shown in Fig. 1(a). Notably, the differential conductance sampled by $V_{\text{THz}}(t)$ may differ from the differential conductance measured by conventional STs even in the absence of photoexcitation [7]. One common difference is that the peak instantaneous current generated in THz-STM experiments tends to exceed typical STM currents by orders of magnitude, e.g., reaching the μA or even mA scale [4,6–8,12]. Figure 1(b) shows the current transient generated by the situation depicted in Fig. 1(a), where the THz voltage transient is applied to a junction defined by the Simmons

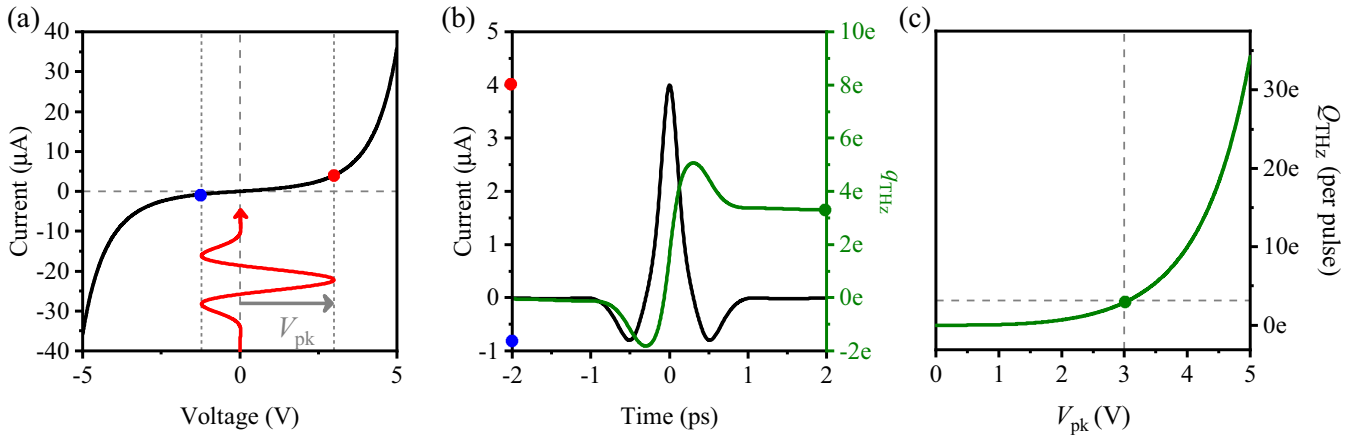


FIG. 1. Terahertz-induced charge rectification across an STM tunnel junction. (a) Simmons model current-voltage (I - V) characteristic (black curve) for a typical THz-STM tip height. In THz-STM, a transient voltage pulse $V_{\text{THz}}(t)$ (represented schematically by red curve) acts on the I - V characteristic. Here, $V_{\text{THz}}(t)$ is defined as a normalized oscillatory component multiplied by V_{pk} . The maximum and minimum voltage sampled by the voltage pulse are indicated by solid red and blue circles, respectively. (b) Ultrafast current pulse (black curve) generated by mapping the transient bias voltage onto the I - V characteristic in (a). Red and blue points indicate the extrema, as in (a). The green curve shows the running integral of the current transient, defined in the text as q_{THz} . The green point denotes the net rectified charge per pulse, defined in the text as Q_{THz} , which is detected in a THz-STM experiment. (c) The simplest spectroscopic measurement for THz-induced tunneling is to sweep V_{pk} and measure Q_{THz} .

model [33,34]. In calculating the Simmons model I - V characteristic, the STM tip height has been reduced compared to conventional STM tip heights, leading to a larger peak current. Such parameters are used in practical THz-STM experiments to account for the relatively low duty cycle (e.g., 10^{-6}) of the train of THz-induced current pulses.

The THz-induced current pulse in Fig. 1(b) is bipolar because the bipolar THz voltage transient accesses sample LDOS features above and below the Fermi level (i.e., at positive and negative voltages, respectively). However, the femtosecond- to picosecond-scale oscillations of the THz-induced current are far too fast to be detected directly by the STM electronics (the bandwidth of a typical STM preamplifier is ≈ 1 kHz). Instead, the electronics measure the net rectified charge across the junction,

$$Q_{\text{THz}} = \int_{-\infty}^{\infty} I(V_{\text{THz}}(t)) dt. \quad (2)$$

Figure 1(b) shows the buildup of the rectified charge during the current pulse, i.e.,

$$q_{\text{THz}}(t') = \int_{-\infty}^{t'} I(V_{\text{THz}}(t)) dt, \quad (3)$$

where Q_{THz} corresponds to the value after the current oscillations are complete (indicated by a green point). Sweeping the THz electric field strength [Fig. 1(c)] traces out the average number of net rectified electrons per THz pulse as a function of V_{pk} . Below, we present an algorithm that utilizes this simple measurement and knowledge of $V_0(t)$ to reconstruct the differential conductance sampled by the THz voltage transient.

III. STEADY-STATE INVERSION ALGORITHM

A. Theory

Inspired by junction-mixing STM [35,36], we model the tunnel current as a polynomial,

$$I(V) = \sum_{n=1}^N A_n V^n, \quad (4)$$

where the A_n terms are constant coefficients. A key difference compared to junction-mixing STM is that lightwave-driven tunneling explores relatively wide voltage ranges at both positive and negative polarity rather than just the local nonlinearity of the I - V characteristic. Hence, the high-order terms of the polynomial series are more important and can even dominate, depending on the voltage and the shape of the I - V curve.

We next consider the rectified charge generated by the THz voltage pulse defined in Eq. (1) acting on the junction (with no DC bias voltage):

$$Q_{\text{THz}}(V_{\text{pk}}) = \sum_{n=1}^N A_n V_{\text{pk}}^n \int_{-\infty}^{\infty} [V_0(t)]^n dt. \quad (5)$$

Knowing the shape of $V_{\text{THz}}(t)$ is essential, as it allows us to calculate a set of coefficients,

$$B_n = \int_{-\infty}^{\infty} [V_0(t)]^n dt, \quad (6)$$

that encapsulate the continuous and bipolar nature of the voltage pulse. Notably, the temporal integral of the free-space electromagnetic pulse that generates $V_{\text{THz}}(t)$ is zero, so $B_1 = 0$. Thus, the contribution to Q_{THz} from the Ohmic part of the

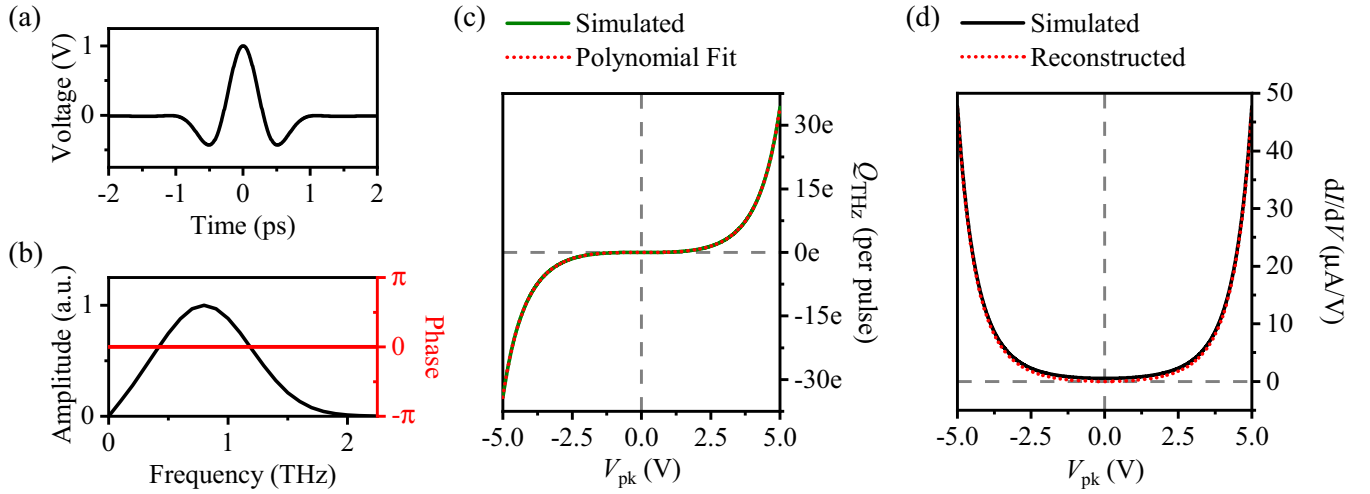


FIG. 2. Reconstructing a Simmons model differential conductance. (a) Simulated THz voltage waveform, $V_0(t)$ and (b) corresponding spectral amplitude (black curve) and phase (red curve). The amplitude is zero at 0 THz, i.e., the temporal integral of $V_0(t)$ is zero. (c) Simulated rectified charge (green curve) for a Simmons model with $\Phi_s = \Phi_t = 5$ eV and polynomial fit of order $N = 22$ (dotted red curve). (d) Simmons model differential conductance (black curve) and reconstructed differential conductance (dotted red curve) obtained from the steady-state inversion algorithm.

conductance is $A_1 B_1 = 0$ and

$$Q_{\text{THz}}(V_{\text{pk}}) = \sum_{n=2}^N C_n V_{\text{pk}}^n, \quad (7)$$

where $C_n = A_n B_n$.

$Q_{\text{THz}}(V_{\text{pk}})$ can be measured directly in a THz-STs experiment. A simulated example is shown in Fig. 1(c). Inverting the polarity of V_{pk} and repeating this sweep allows the full function to be mapped out. Within the algorithm introduced here, $Q_{\text{THz}}(V_{\text{pk}})$ is simply fit with a polynomial to extract the coefficients C_n , which can subsequently be combined with the B_n coefficients determined by numerical integration of the measured voltage transient to yield the I - V characteristic:

$$I(V_{\text{pk}}) = A_1 V_{\text{pk}} + \sum_{n=2}^N \frac{C_n}{B_n} V_{\text{pk}}^n. \quad (8)$$

A limitation of steady-state THz-STs is that the Ohmic part of the conductance does not produce a rectified charge, and therefore the A_1 term is inaccessible. However, calculating the differential conductance,

$$\frac{dI}{dV_{\text{pk}}}(V_{\text{pk}}) = A_1 + \sum_{n=2}^N n \frac{C_n}{B_n} V_{\text{pk}}^{n-1}, \quad (9)$$

reduces the missing Ohmic contribution to a constant offset. For simplicity, we set $A_1 = 0$ in the following.

B. Demonstration

Here, we demonstrate the steady-state algorithm's effectiveness by recovering the differential conductances of model systems from simulated THz-STs data. The simple THz voltage waveform shown in Fig. 2(a) is used for the THz-STs simulations. The spectral amplitude and phase of the pulse are shown in Fig. 2(b).

The algorithm is, in principle, independent of the precise shape of the waveform, but we note that a perfectly symmetric waveform (i.e., sinelike, with $\phi_{\text{CEP}} = \pm\pi/2$) leads to ambiguity, since changing the polarity does not impact Q_{THz} , i.e., $Q_{\text{THz}}(V_{\text{pk}}) = Q_{\text{THz}}(-V_{\text{pk}})$. This can be seen by isolating the even and odd order terms in Eq. (7). In general, $Q_{\text{THz}}(V_{\text{pk}}) + Q_{\text{THz}}(-V_{\text{pk}})$ can be fit by a polynomial with only the terms of even n , while $Q_{\text{THz}}(V_{\text{pk}}) - Q_{\text{THz}}(-V_{\text{pk}})$ can be fit by a polynomial with only the terms of odd n . However, for a perfectly symmetric pulse, $Q_{\text{THz}}(V_{\text{pk}}) - Q_{\text{THz}}(-V_{\text{pk}}) = 0$ for any I - V curve, so the odd order terms of the polynomial are inaccessible. In other words, inverting the waveform does not change the weighting between I - V features at positive and negative V , so the I - V asymmetry and curvature cannot be disentangled. Optimistically, any asymmetry in $V_{\text{THz}}(t)$ introduces sensitivity to the odd order terms in Eq. (7), but, realistically, the asymmetry should significantly exceed the noise level. The waveform shape, $V_0(t)$, in Fig. 1(a) can therefore be considered ideal in that it is optimally asymmetric ($\phi_{\text{CEP}} = 0$).

The first example considered is a Simmons model with material and tip work functions of $\Phi_s = 5$ eV and $\Phi_t = 5$ eV, respectively. The rectification process for this scenario is sketched in Fig. 1. To apply the steady-state inversion algorithm, the V_{pk} sweep is performed for both $V_{\text{pk}} < 0$ and $V_{\text{pk}} > 0$, then the complete $Q_{\text{THz}}(V_{\text{pk}})$ (solid green curve) is fit by a polynomial (with $C_1 = 0$; dotted red curve) to obtain the $C_{n>1}$ coefficients, as shown in Fig. 2(c). Meanwhile, the B_n coefficients are calculated by numerical integration of the THz voltage waveform raised to the n th power, as defined in Eq. (6). Finally, the differential conductance extracted through the algorithm can be computed directly based on the C_n and B_n coefficients via Eq. (9). As noted above, we set $A_1 = 0$ because this term cannot be determined from the algorithm when $B_1 = 0$. Figure 2(d) shows a comparison between the differential conductance of the Simmons model used in the simulation (solid black curve) and the differential conductance

reconstructed from the algorithm (dotted red curve). We note that the voltage axis of Fig. 2(d) is labeled V_{pk} for consistency with the algorithm, whereas the original is plotted as $dI(V_{pk})/dV_{pk}$ for comparison, but is, strictly speaking, a function of V . The agreement is near perfect aside from a vertical offset corresponding to A_1 .

In general, the algorithm performs exceptionally well for any I - V characteristic that can be well described by a low-order polynomial. Furthermore, for polynomials with $A_1 = 0$, the offset disappears and the reconstructed differential conductance matches the original. However, experimental differential conductances are often nonmonotonic, e.g., due to resonances in the sample LDOS, and can require higher polynomial orders to reasonably reproduce them. Therefore, we next test the algorithm for highly nonlinear I - V characteristics corresponding to model physical systems.

We first model a semiconducting sample with band onsets at -1.5 V and $+1.5$ V bias. Figure 3(a) shows the I - V characteristic (top, solid black curve) and differential conductance (bottom, solid black curve). The latter is modeled as the sum of two error functions, one for each band. Simulating charge rectification by the THz waveform in Fig. 2(a) yields the dotted red curve in Fig. 3(a), top, which qualitatively resembles the I - V curve. Applying the steady-state inversion algorithm, i.e., determining B_n and C_n and then calculating $dI(V_{pk})/dV_{pk}$ using Eq. (9), yields a reconstructed differential conductance [Fig. 3(a), bottom, dotted red curve] that matches the original.

Figure 3(b) shows another example, this time corresponding to peaks in the sample LDOS such as those observed for single molecules adsorbed on salt islands [5,11,13,37]. We model the differential conductance with Gaussians peaked at ± 2 V [Fig. 3(b), bottom, solid black curve], and hence the I - V characteristic is the sum of two error functions [Fig. 3(b), top, solid black curve]. The rectified charge [Fig. 3(b), top, dotted red curve] diverges more strongly from the shape of the I - V curve in this case, but the algorithm once more accurately reconstructs the differential conductance [Fig. 3(b), bottom, compare dotted red and solid black curves].

C. Simulated experiment

To test our algorithm's robustness and stability, we introduce noise and simulate an experimental THz-STs measurement. We model noise based on pulse-to-pulse energy fluctuations in a near-infrared laser system, which generates THz pulses through optical rectification. Since the emitted THz field is proportional to near-infrared pulse energy, these fluctuations produce a pulse-to-pulse variation in the strength of the THz voltage applied across the junction. We model this by $V_{THz}(t) = (1 \pm \epsilon)V_{pk}V_0(t)$, where ϵ is a random number chosen from within a range defined by the near-infrared pulse fluctuations. For our simulations, $\epsilon_{max} = 0.05$. The absolute voltage uncertainty grows with V_{pk} , e.g., for $|V_{pk}| = 3$ V the uncertainty range is 0.3 V. Notably, the entire THz voltage waveform scales with the near-infrared pulse energy, as it is expected to retain its temporal shape in an experiment provided the nonlinear generation crystal does not change.

An example of the simulated experiment is shown in Fig. 4(a), where ten noisy $Q_{THz}(V_{pk})$ curves are overlaid, forming the grey region, which expands with increasing $|V_{pk}|$.

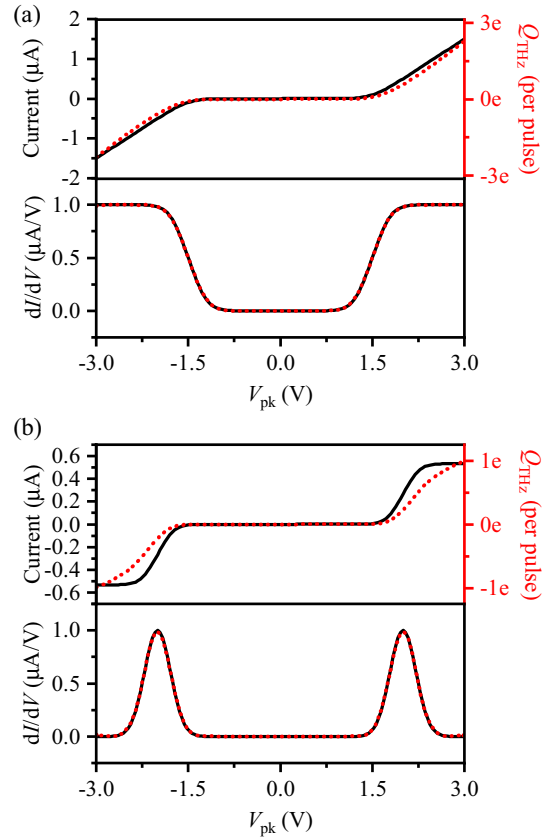


FIG. 3. Reconstructing highly nonlinear differential conductances. (a) Top: I - V characteristic for a simple model of a semiconducting sample with band onsets at -1.5 V and $+1.5$ V (black curve) and corresponding rectified charge (dotted red curve) produced by the THz voltage waveform in Fig. 2(a). Bottom: Differential conductance for the semiconductor model (black curve) and reconstructed differential conductance (dotted red curve). (b) Top: I - V characteristic for a simple model of a molecule adsorbed on a salt film on a metal substrate with orbital transport resonances centered at ± 2 V (solid black curve) and corresponding rectified charge (dotted red curve) produced by the THz voltage waveform in Fig. 2(a). Bottom: Differential conductance for the molecular system (solid black curve) and reconstructed differential conductance (dotted red curve). Fitting of $Q_{THz}(V_{pk})$ in each system was performed with a polynomial of order $N = 38$.

This effect is mitigated by standard measurement techniques, where the rectified charge of many pulses is averaged by a lock-in amplifier. The average of the ten $Q_{THz}(V_{pk})$ curves is shown as the red curve in Fig. 4(a). Its roughness is comparable to similar data sets from the literature [7]. Unfortunately, the noise in even the average curve leads to spurious weighting of high order polynomial terms in the fitting step of the algorithm. This, in turn, can result in unphysical oscillations in the extracted differential conductance. Therefore, it is necessary to develop a procedure to obtain a reliable result.

While it is possible to employ an arbitrarily large number of polynomial orders, limiting the number of terms to avoid overfitting noisy data can suppress oscillations in the extracted dI/dV curve. Nevertheless, we find that polynomials with order greater than five tend to develop undesirable dI/dV

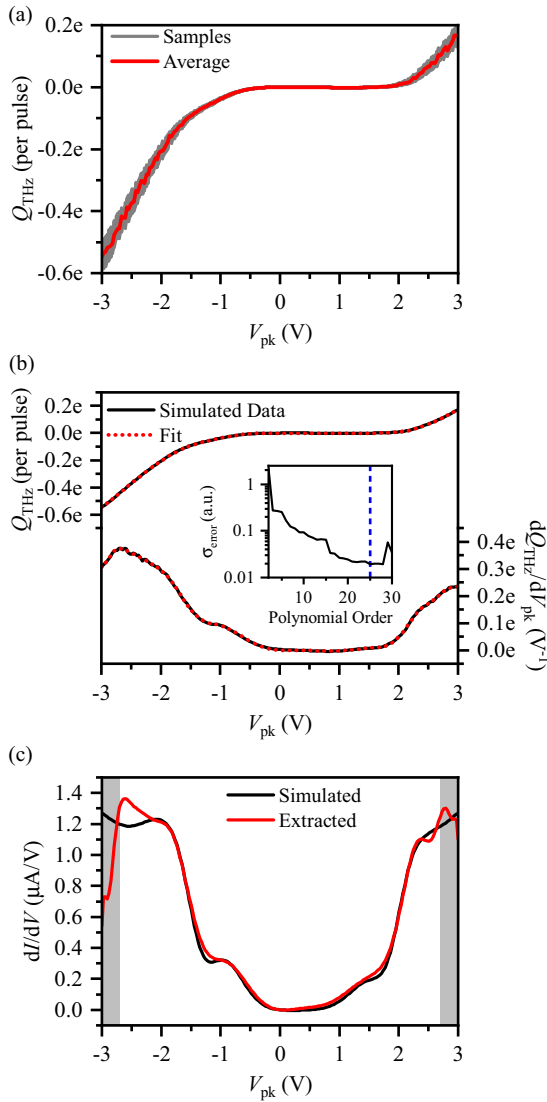


FIG. 4. Reconstructing an arbitrary differential conductance in the presence of noise. (a) In a simulated THz-STs experiment, charge rectification is calculated for a voltage waveform with a randomly fluctuating field strength ($\epsilon_{\max} = 0.05$; 10 calculations per V_{pk}). The grey region shows the simulated experimental data and the red curve is the average. (b) $Q_{\text{THz}}(V_{\text{pk}})$ (top black curve) and $dQ_{\text{THz}}(V_{\text{pk}})/dV_{\text{pk}}$ (bottom black curve) after a Savitzky-Golay filter of order 1 has been applied with a window of 0.27 V ($\sim 5\%$ of the V_{pk} axis width). Dotted red curves: Simultaneous fit. Inset: Standard deviation of the fit to $Q_{\text{THz}}(V_{\text{pk}})$. Dashed blue line: Polynomial order used for the fits in (b) and extraction in (c). (c) Comparison between the simulated differential conductance (black curve) and the algorithm result (red curve) for polynomial of order $N = 25$. Grey vertical bars: $\sim 5\%$ of the axis width, where the filters break down.

oscillations at the edges of the voltage range when the algorithm is applied as described in the previous section to noisy $Q_{\text{THz}}(V_{\text{pk}})$ data. However, we have discovered that simultaneously fitting both $Q_{\text{THz}}(V_{\text{pk}})$ and $dQ_{\text{THz}}(V_{\text{pk}})/dV_{\text{pk}}$ when finding C_n better constrains the behavior at the boundaries. To obtain a well-behaved numerical derivative, a smoothing function is applied to $Q_{\text{THz}}(V_{\text{pk}})$ prior to calculating $dQ_{\text{THz}}(V_{\text{pk}})/dV_{\text{pk}}$. A second smoothing function is applied to

$dQ_{\text{THz}}(V_{\text{pk}})/dV_{\text{pk}}$ to reduce the noise that is introduced when calculating the derivative. The smoothed data [Fig. 4(b), black curves] are produced by applying a Savitzky-Golay filter in each step [38] that convolutes a linear polynomial with a moving window that is $\sim 5\%$ of the total V_{pk} range (i.e., ~ 0.3 V).

To determine an appropriate number of polynomial fit terms, we calculate the standard deviation, σ_{error} , between the fit result and $Q_{\text{THz}}(V_{\text{pk}})$ as a function of fit order. The polynomial fits in Fig. 4(b) (dotted red curves) use a polynomial in the lowest plateau region of σ_{error} [marked by a dashed blue line in the inset of Fig. 4(b)]. Although limiting the number of polynomial orders used in the fit reduces the voltage resolution in the extracted differential conductance, it also increases the stability and reliability of the result.

In Fig. 4(c), we compare the simulated differential conductance (black curve) to the extracted differential conductance (red curve) following this procedure. We have used a more structured model dI/dV here than those shown in the previous section to better approximate a real experiment. It is important to note the smoothing filters overshoot at the boundaries of $Q_{\text{THz}}(V_{\text{pk}})$ and $dQ_{\text{THz}}(V_{\text{pk}})/dV_{\text{pk}}$, so the extracted dI/dV in this region (grey shaded area) may still contain oscillations, as is the case here. The tradeoff between polynomial order and resolution is apparent in the features near ± 1 V, both of which are broadened. Nevertheless, the adapted algorithm outlined in this section successfully reproduces the salient features of the differential conductance in the presence of noise while mostly constraining artifacts to the $\sim 5\%$ of the voltage range nearest the boundaries.

Including more derivatives in the simultaneous fit can further suppress oscillations, but further smoothing is also required for each additional derivative order. Employing a more sophisticated technique to handle the derivatives of noisy data (e.g., regularization) may improve this approach. We have also explored other procedures (e.g., matrix multiplication, frequency filtering, etc.), but their compatibility with the time-dependent algorithm of the next section has not yet been shown, so it is difficult to comment on their effectiveness at this time.

IV. TIME-DEPENDENT INVERSION ALGORITHM

A. Theory

The previous section outlined an algorithm to reconstruct static differential conductances from THz-STs measurements. However, a THz voltage pulse can also probe the ultrafast evolution of the junction following photoexcitation by a femtosecond optical or near-infrared pump pulse, as illustrated in Fig. 5(a).

In such an experiment, absorption of the pump pulse modifies the junction, changing the I - V characteristic on the timescale of its intensity envelope. The I - V curve subsequently decays back to the ground state on a timescale defined by the material system. The time-delayed THz probe pulse samples this evolution by adiabatically sweeping through voltage configurations. In this section, we assume THz-driven tunneling does not affect the time dependence of the I - V characteristic. Meanwhile, our treatment of the THz probe as quasistatic is justified by the Keldysh parameter ($\gamma \ll 1$).

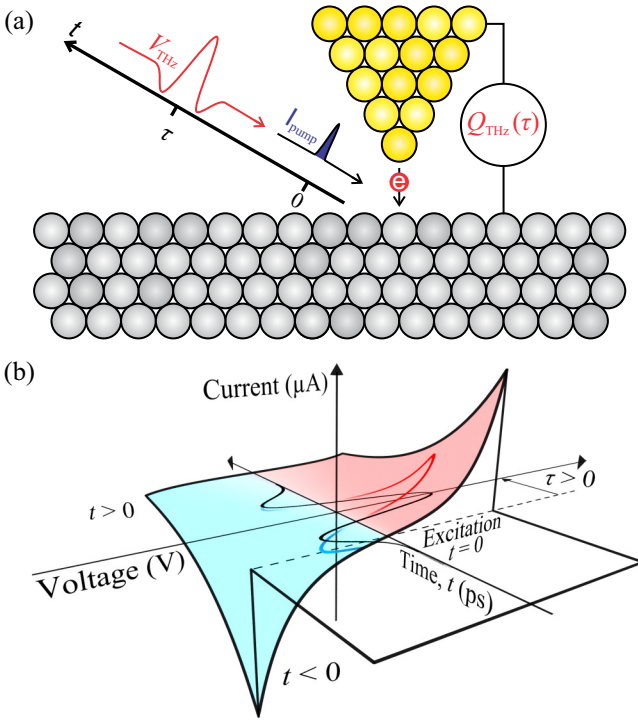


FIG. 5. Visualizing pump-probe THz-STIS of a transient I - V characteristic. (a) Schematic depicting an optical-pump/THz-STIS-probe measurement. The pump pulse is absorbed by the sample at $t = 0$, triggering a modification of the I - V characteristic within the pump intensity envelope (I_{pump}). The evolution of the junction is read out via the rectified current [$Q_{\text{THz}}(\tau)$] generated by a time-delayed THz voltage probe (V_{THz}). (b) In an example pump-probe THz-STIS experiment, a Simmons model I - V curve is initialized at $t = 0$ by optical excitation and subsequently decays with a decay time of 1 ps. A THz voltage pulse (black curve) arrives at the tunnel junction after a delay time τ , where τ is defined as the time from excitation to the peak of $V_{\text{THz}}(t)$ and is positive (negative) when the optical pulse arrives first (second). Red and blue shading denotes positive and negative currents, respectively. The THz voltage pulse is mapped onto the time-dependent I - V curve (red and blue curve), indicating the THz-induced trajectory through three-dimensional I - V - t space. Notably, the THz-induced current is larger for oscillations occurring soon after photoexcitation.

Figure 5(b) depicts the projection of $V_{\text{THz}}(t)$ onto a time-dependent I - V curve defined by a Simmons model that appears at $t = 0$ and decays exponentially for $t > 0$ with a $1/e$ time of 1 ps. We define the delay time τ as the time from photoexcitation (at $t = 0$) to the arrival of the THz voltage peak. The dynamics are encoded in the resulting THz-induced current transient, which depends on t and τ , while detection via the rectified charge (after integration over t) further obscures the sample dynamics. We note that the rectified charge retains its dependence on τ , since the pump-probe experiment can be repeated for different τ to generate $Q_{\text{THz}}(\tau)$. In the following, we introduce an algorithm to reconstruct the time-dependent differential conductance of a tunnel junction from $Q_{\text{THz}}(V_{\text{pk}}, \tau)$ in a pump-probe experiment.

We begin by generalizing the static I - V polynomial from Sec. III to a dynamic polynomial with arbitrary temporal

structure. This is done through time-dependent series coefficients, i.e.,

$$I(V, t) = \sum_{n=1}^N A_n(t) V^n. \quad (10)$$

Substituting $I(V, t)$ into the expression for rectified charge [analogous to Eq. (5) in the previous section] yields

$$Q_{\text{THz}}(V_{\text{pk}}, \tau) = \sum_{n=1}^N V_{\text{pk}}^n \int_{-\infty}^{\infty} A_n(t + \tau) [V_0(t)]^n dt. \quad (11)$$

Unlike in the static case, the coefficients of the polynomial cannot be moved outside the temporal integral. Nevertheless, the rectified charge $Q_{\text{THz}}(V_{\text{pk}}, \tau)$ can still be written as a polynomial:

$$Q_{\text{THz}}(V_{\text{pk}}, \tau) = \sum_{n=1}^N C_n(\tau) V_{\text{pk}}^n. \quad (12)$$

We highlight that the series in Eqs. (11) and (12) begins at $n = 1$, whereas the static $Q_{\text{THz}}(V_{\text{pk}})$ polynomial in Sec. III began at $n = 2$ [Eq. (7)] because a nonzero rectified charge can be generated by an Ohmic component that changes with time.

The experimental protocol for pump-probe THz-STIS is to record a $Q_{\text{THz}}(V_{\text{pk}}, \tau)$ map. For each sweep of V_{pk} (i.e., for each τ), $Q_{\text{THz}}(V_{\text{pk}})$ is fit by a polynomial, similar to the procedure in the steady-state algorithm. Repeating this process as a function of τ allows $C_n(\tau)$ to be determined experimentally, where

$$C_n(\tau) = \int_{-\infty}^{\infty} A_n(t + \tau) [V_0(t)]^n dt. \quad (13)$$

Here, we note that $C_n(\tau)$ is a cross correlation of $A_n(t)$ and $[V_0(t)]^n$, and therefore these functions can be isolated using the cross-correlation theorem (which is similar to the convolution theorem). Specifically,

$$\mathcal{F}\{C_n(\tau)\}(v) = \mathcal{F}\{A_n(t)\}(v) \times \mathcal{F}\{[V_0(t)]^n\}(v). \quad (14)$$

Utilizing a numerical fast Fourier transform algorithm allows $\mathcal{F}\{C_n\}(v)$ and $\mathcal{F}\{V_0^n\}(v)$ to be extracted from the experimental $C_n(\tau)$ and $V_0(t)$, respectively. Thus, $A_n(t)$ can be obtained by

$$A_n(t) = \mathcal{F}_v^{-1} \left\{ \frac{\mathcal{F}\{C_n\}(v)}{\mathcal{F}\{V_0^n\}(v)} \right\}, \quad (15)$$

where each n term is calculated separately. A consequence of Eq. (15) is that the accessible $A_n(t)$ bandwidth depends on the bandwidth of $[V_0(t)]^n$, which in turn is a function of n . This impacts the time resolution of THz-STIS, especially in the subcycle regime, as discussed in the following sections.

Within the bandwidth limits, Eq. (15) directly yields the coefficients of the time-dependent polynomial in Eq. (10), including the Ohmic term. The time-dependent differential conductance can be obtained from

$$\frac{dI}{dV_{\text{pk}}}(V_{\text{pk}}, t) = \sum_{n=1}^N n A_n(t) V_{\text{pk}}^{n-1}. \quad (16)$$

In contrast to the steady-state algorithm, Eq. (16) includes even the $n = 1$ term, which is independent of voltage, because its time dependence brings it into view for THz-STIS.

In the following section, we will demonstrate the algorithm's efficacy by extracting the time-dependent differential conductance from simulated pump-probe THz-STS experiments.

B. Demonstration

We demonstrate the time-dependent algorithm's effectiveness by recovering a dynamic differential conductance, which we conceive as a model for a photoexcited semiconductor. We describe the differential conductance of the unexcited sample with two error functions, representing conduction and valence bands, with onsets at +2 V and -1 V, respectively. We then introduce ultrafast optical excitation at $t = 0$: A pump pulse with photon energy of 3 eV redistributes electrons from the valence band to the conduction band. The subsequent decay dynamics are imprinted on the time-dependent I - V characteristic, but the precise behavior is nontrivial and depends on the sample. For the simple case considered here, we speculate that the dominant change may arise from field emission of electrons from the conduction band. We therefore incorporate a transient, one-sided Simmons model with a sample work function of $\Phi_s = 3$ eV that appears instantaneously at $t = 0$ ps and decays with a $1/e$ time of 1 ps. The value of Φ_s is chosen to model field emission from states well above the Fermi level, i.e., Φ_s is smaller than a typical material work function, while the decay time represents a generic reduction in electrons available for field emission over time, for example, through a combination of electron-hole recombination, carrier trapping, and depletion layer formation at the surface [39].

Although the $I(V, t)$ considered here is an example created to demonstrate the time-dependent algorithm's effectiveness, it may be informative to add a few general comments: (i) Optical excitation will likely produce photocurrent even for zero bias voltage, which corresponds to a finite $n = 0$ term in $I(V, t)$. However, this photocurrent is neglected here because THz-STS measurements recorded via lock-in detection, where the THz pulse train is modulated, are insensitive to currents that do not depend on $V_{\text{THz}}(t)$. (ii) Tunneling into the conduction band and out of the valence band will presumably also be modulated to some extent by photoexcitation, but we assume that the corresponding impact on the differential conductance will be minor because the fraction of electrons that are photoexcited is likely to be small. Yet, this assumption may break down if the sample contains only a few electrons. (iii) Our time-dependent Simmons model incorporates photo-assisted field emission only from the sample and neglects a similar process from a photoexcited tip. Meanwhile, field emission at the sample and tip work functions is considered to be present, but it is assumed to be negligible here and is therefore left out of the model.

Figure 6(a) shows $Q_{\text{THz}}(V_{\text{pk}}, \tau)$ generated in a simulated pump-probe THz-STS experiment based on the $I(V, t)$ described above and the waveform in Fig. 2(a). Interestingly, whereas the shape of $Q_{\text{THz}}(V_{\text{pk}})$ for the static semiconductor model in Fig. 3(a) resembled that of $I(V)$, their time-dependent shapes in the pump-probe simulation can strongly differ. At $V_{\text{pk}} = 4$ V [Fig. 6(b)], $Q_{\text{THz}}(\tau)$ features two prominent negative peaks spaced by 1 ps and an approximately exponential decay for $\tau > 2$ ps (red circles), despite there being no time dependence in $I(V, t)$ at $V = 4$ V at all (black

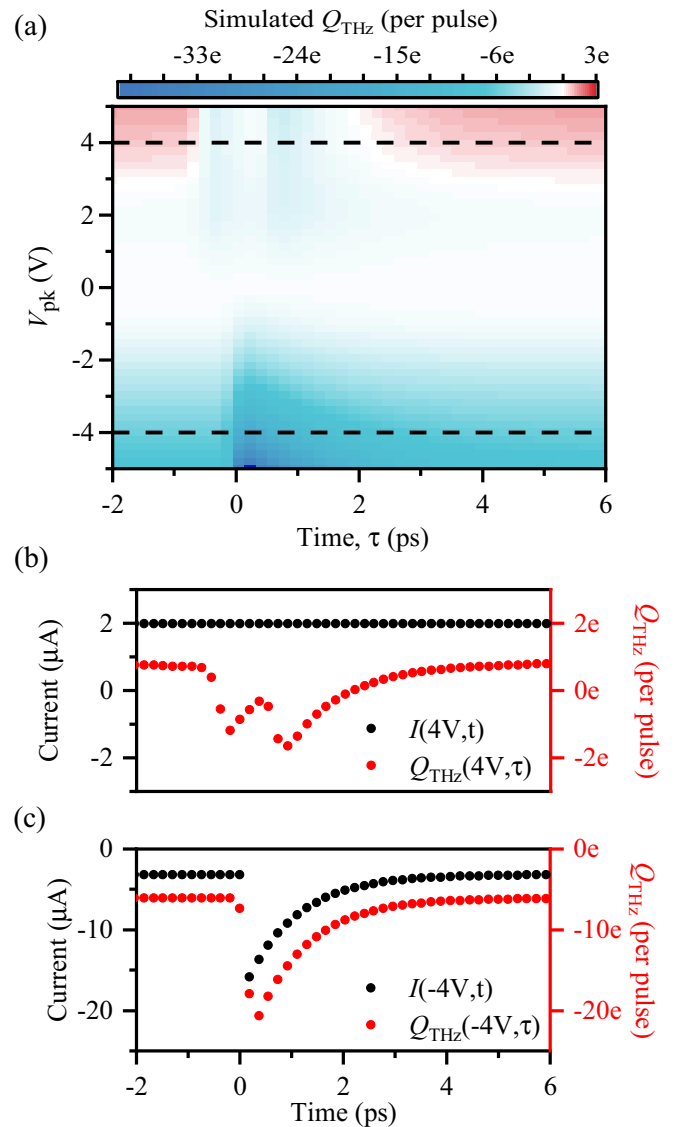


FIG. 6. Simulated pump-probe THz-STS data. The simulation is performed using the THz voltage waveform in Fig. 2(a) and the time-dependent differential conductance model described in the text, where the definition of the delay time τ is shown in Fig. 5(b). (a) Rectified charge map produced by the simulation. The algorithm was applied to a τ window from -5 ps to 15 ps; a cropped region is presented to highlight detail on the subpicosecond timescale. Dashed lines are guides indicating the cross-sectional cuts shown in (b) and (c). (b) Cut through the rectified charge map at $V_{\text{pk}} = 4$ V (red circles) and simulated $I(V, t)$ at $V = 4$ V for comparison (black circles). (c) Cut through the rectified charge map at $V_{\text{pk}} = -4$ V (red circles) and simulated $I(V, t)$ at $V = -4$ V for comparison (black circles).

circles). Conversely, at $V_{\text{pk}} = -4$ V [Fig. 6(c)], the $Q_{\text{THz}}(\tau)$ transient (red circles) is similar to $I(t)$ (black circles), i.e., the decay of the rectified charge is a reasonable proxy for the inherent dynamics of the junction. Together, Figs. 6(b) and 6(c) illustrate that although THz-STS can in some circumstances directly capture the dynamics of the junction, convolution of the THz voltage waveform with those dynamics can also produce misleading features in the experimental data. Furthermore, the parameter space in which each effect

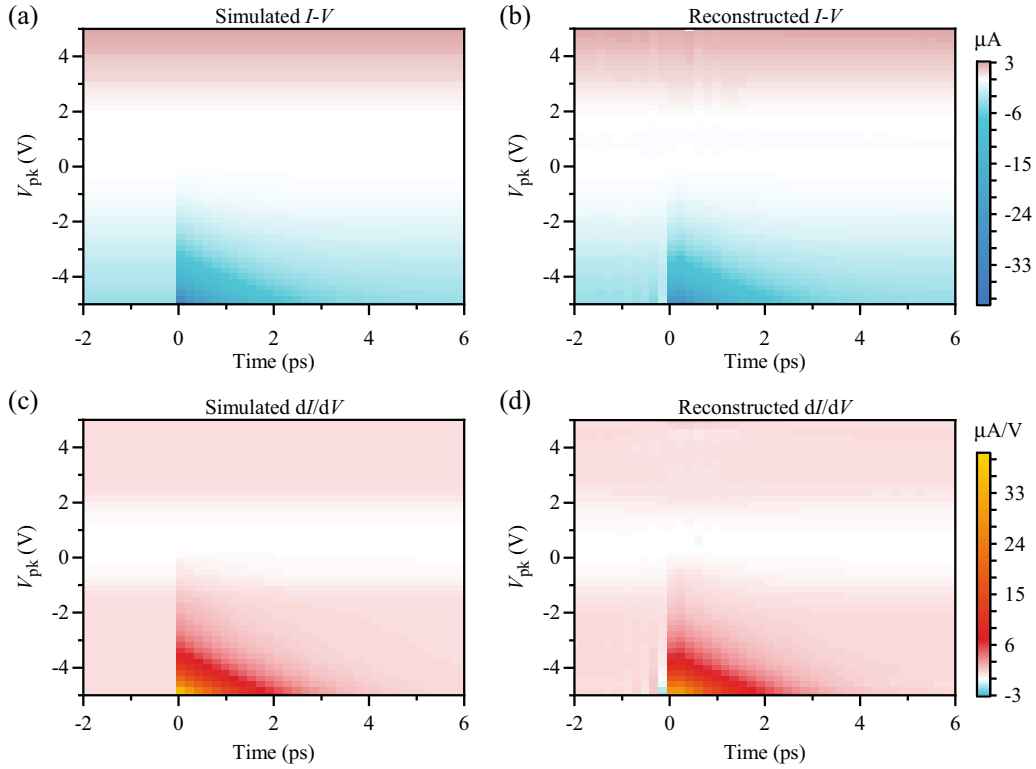


FIG. 7. Reconstructing a transient I - V curve and differential conductance with the time-dependent inversion algorithm. (a) Original I - V characteristic used to simulate the THz-STs data shown in Fig. 6(a). (b) Reconstructed I - V characteristic obtained using the time-dependent inversion algorithm. (c) Differential conductance for the model tunnel junction in (a). (d) Reconstructed differential conductance determined alongside (b) using the inversion algorithm. Fitting of $Q_{\text{THz}}(V_{\text{pk}})$ in the algorithm was performed with a polynomial of order $N = 21$. All plots are cropped along the time axis from the original bounds of -5 ps to 15 ps.

dominates is not obvious *a priori*, meaning there is significant uncertainty whether $Q_{\text{THz}}(V_{\text{pk}}, \tau)$ shows the intrinsic behavior of the junction for a particular choice of V_{pk} . An algorithm that reveals $I(V, t)$ using the entire $Q_{\text{THz}}(V_{\text{pk}}, \tau)$ map is therefore essential for pump-probe THz-STs.

Here, we apply the pump-probe THz-STs inversion algorithm introduced in the previous section to the $Q_{\text{THz}}(V_{\text{pk}}, \tau)$ map in Fig. 6(a). The original $I(V, t)$ used to generate the map is shown in Fig. 7(a). The procedure is as described in the previous section. Briefly, $Q_{\text{THz}}(V_{\text{pk}}, \tau)$ is fit by a polynomial at each time step, as defined in Eq. (12). The n th-order coefficients form a time-dependent function, $C_n(\tau)$. The Fourier transform of $C_n(\tau)$ is divided by the Fourier transform of $[V_0(t)]^n$, and the inverse Fourier transform of the result yields the $A_n(t)$ coefficients of the polynomial. In practice, we also employ an amplitude cutoff for $\mathcal{F}\{V_0^n\}(\nu)$ to avoid divergences, which we set to 5×10^{-4} . For any $\mathcal{F}\{V_0^n\}(\nu)$ below the cutoff, $\mathcal{F}\{A_n\}(\nu)$ is set to 0. The resulting reconstructed $I(V, t)$ obtained through the algorithm is shown in Fig. 7(b). It agrees remarkably well with the original. The simulated and reconstructed differential conductances are shown in Figs. 7(c) and 7(d), respectively, where the agreement is once more exemplary.

We have further tested the time-dependent algorithm for decay times of 10 ps and 100 ps and found the accuracy of the reconstruction to be similar or better. Alternatively, the steady-state algorithm may be applied to transient I - V characteristics

with decay times greater than 10 ps to similar effect (provided the region near $\tau = 0$ ps is excluded) since the differential conductance changes slowly during the oscillations of the THz voltage pulse. For yet longer decay times, e.g. greater than 100 ps, the steady-state algorithm is recommended, as the sample dynamics are dominated by frequency components below the THz pulse bandwidth. These frequencies are excluded from the inversion calculation through the $\mathcal{F}\{V_0^n\}(\nu)$ amplitude cutoff.

C. Subcycle time resolution

The time-dependent inversion algorithm is capable of extracting dynamics faster than a single oscillation cycle of the THz voltage probe. This subcycle time resolution is evident in Fig. 7, where the algorithm reproduces the stepwise onset of the transient at $t = 0$, in addition to the exponential decay for $t > 0$. The onset of the simulated transient occurs in a single 200 fs timestep, i.e., at a rate exceeding the 2 THz bandwidth of the voltage probe [Fig. 2(b)].

We explore the time resolution of the algorithm further using a simple symmetric Simmons model ($\Phi_s = \Phi_t = 5$ eV) that appears at $t = 0$ and decays exponentially for $t > 0$, as illustrated in Fig. 5(b). For $t < 0$, $I = 0$ for all V . We consider the case of a 1 ps decay time and an onset that occurs in one 80 fs time step. Figure 8(a) shows slices through $dI(V, t)/dt$ at constant voltages of -5 V, -3 V, and -1 V along with

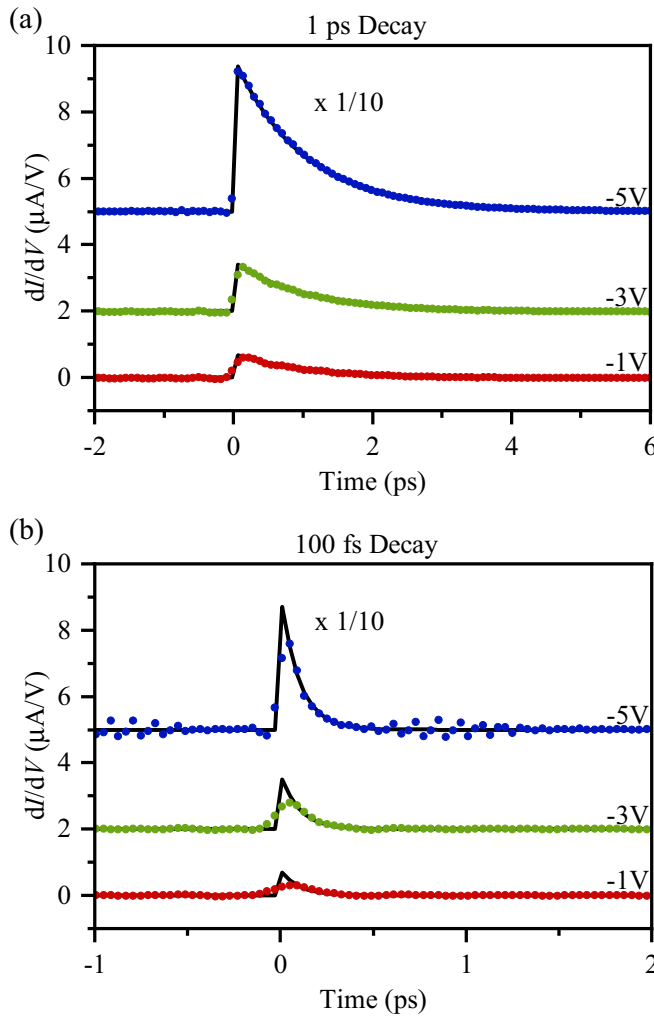


FIG. 8. Resolving subcycle dynamics with the time-dependent inversion algorithm. The simulated I - V characteristic is defined by a Simmons model that appears at $t = 0$ and subsequently decays away exponentially for $t > 0$, as described in the text. For $t < 0$, $I = 0$ and $dI/dV = 0$. (a), (b) Simulated transient differential conductance at $V = -5$ V, $V = -3$ V, and $V = -1$ V (black curves, offset for clarity) for a decay time of (a) 1 ps and (b) 100 fs. The reconstructed transient differential conductance is shown for the same voltages ($V_{\text{pk}} = -5$ V: blue circles; $V_{\text{pk}} = -3$ V: green circles; $V_{\text{pk}} = -1$ V: red circles). Fitting $Q_{\text{THz}}(V_{\text{pk}})$ in the time-dependent algorithm was performed with a polynomial of order $N = 21$ for both 1 ps and 100 fs calculations. In both panels, the plots are cropped from the original time axis of -5 ps to 15 ps that was used in the time-dependent algorithm. Panel (b) was calculated using 500 points along the time axis compared to 250 points for panel (a) to facilitate analysis at higher frequencies.

the corresponding cuts through the reconstruction result. The algorithm reproduces the 1 ps exponential decay of the differential conductance at all voltages. Conversely, the 80 fs onset of the transient is only well reproduced for the highest magnitude bias (-5 V), whereas the onset is broadened for voltages closer to 0 (-3 V, -1 V). Interestingly, this means that the step width is better resolved for larger step heights.

The algorithm's time resolution at a given voltage is linked to the nonlinearity of the I - V characteristic at that voltage.

Conceptually, this can be understood by considering the THz-induced current pulse. For the case of the Simmons model, the current rapidly increases (decreases) as the voltage reaches the work function of the tip (sample). Therefore, for V_{pk} approaching a work function, the full width at half maximum of the current produced by the main $V_{\text{THz}}(t)$ oscillation cycle narrows. Meanwhile, within the time-dependent algorithm, the fit to $Q_{\text{THz}}(V_{\text{pk}}, \tau)$ [see Eq. (12)] is dominated at low V_{pk} by low polynomial orders and at high V_{pk} by high polynomial orders. The result is faster time resolution for the higher order terms in the inversion algorithm and, similarly, faster time resolution for the parts of the reconstructed differential conductance at higher $|V_{\text{pk}}|$. This explains why the reconstructed step widths in Fig. 8(a) narrow with increasing $|V_{\text{pk}}|$. It further implies that yet faster time resolution can be achieved for highly nonlinear I - V curves.

We explore the limits of the algorithm's subcycle time resolution by examining a transient Simmons model that appears within one 40 fs time step ($1/40$ fs = 25 THz) and decays with a time constant of 100 fs ($1/100$ fs = 10 THz). For comparison, the spectral amplitude of the THz voltage pulse is negligible above 2 THz [Fig. 2(b)]. Figure 8(b) shows cuts through the differential conductance at -1 V, -3 V, and -5 V alongside cuts through the reconstructed differential conductance at the same voltages. As expected, the time resolution improves for increasing $|V_{\text{pk}}|$, with the result at -5 V close to matching the onset and decay rate, though with lower overall amplitude. However, the reconstructed curve for -5 V also, surprisingly, includes oscillations at both negative and positive times that are not present in the original curve.

The relative accuracy of the reconstructed differential-conductance transients can be understood by considering how subcycle time resolution arises in Eq. (15). The bandwidth of $[V_0(t)]^n$ increases for increasing n , as shown in Fig. 9(a). The spectral amplitude above the cutoff [dashed black line in Fig. 9(a)] defines the maximum frequency (ν_n) that can be resolved at a given n . Within the time-dependent algorithm, $\mathcal{F}\{A_n\}(\nu)$ is set to zero for frequencies above ν_n , so the reconstructed differential conductance contains the corresponding order only for frequencies below ν_n . This loss of information is visualized in Figs. 9(b) and 9(c), which show the spectral amplitudes of the cuts through the simulated and reconstructed differential conductances from Figs. 8(a) and 8(b), respectively. At the frequencies indicated by the grey lines, the amplitude of $\mathcal{F}\{[V_0]^n\}(\nu)$ crosses the cutoff threshold [Fig. 9(a)] and that order is dropped from the reconstructed differential conductance [discontinuities in Figs. 9(b) and 9(c)]. Only odd orders have a significant impact in this example because the I - V curve is antisymmetric and therefore composed of only odd-order terms.

The loss of information is most impactful for the reconstructed curves at low V_{pk} [e.g., -1 V in Figs. 9(a) and 9(b)], since the $A_{n < 5}$ coefficients dominate. Conversely, at -5 V, the I - V characteristic is more nonlinear, and hence is composed primarily of higher order terms, so dropping A_1 , for example, does not lead to much deviation from the simulated amplitude. Meanwhile, the 1 ps decay curve is better reproduced in the time domain than the 100 fs decay curve [compare Fig. 8(a) to 8(b)]. This is because the amplitude of the simulated differential conductance is weighted more strongly at frequencies

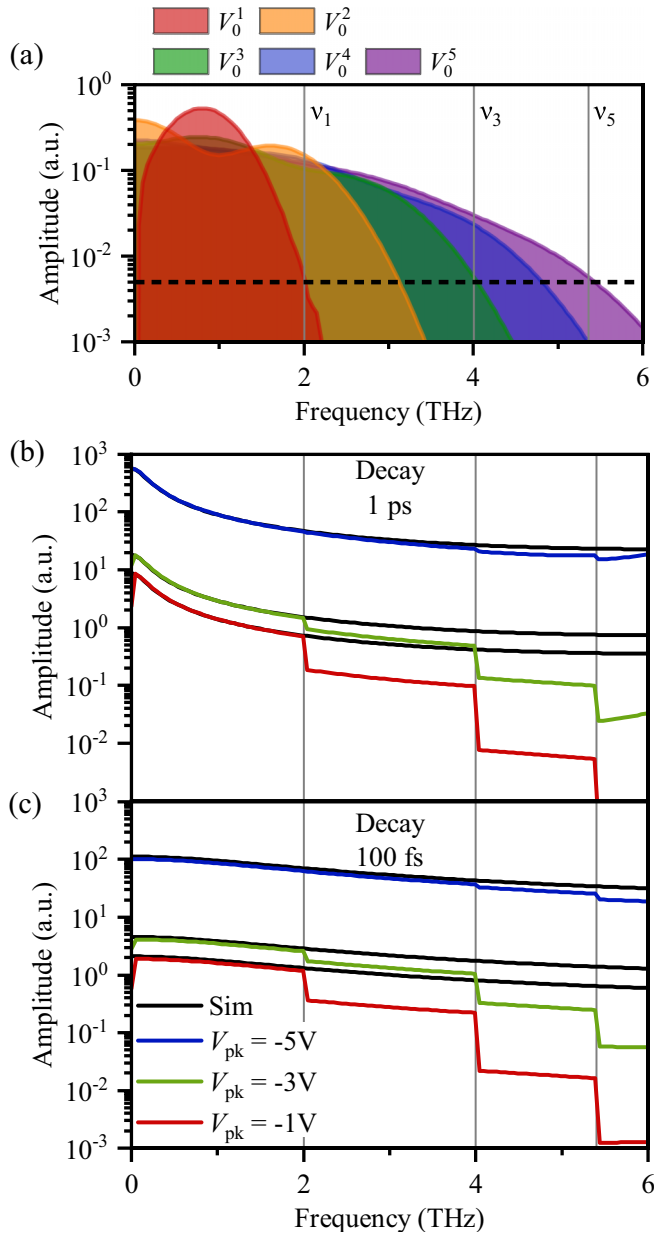


FIG. 9. Defining the time resolution of THz-STs. (a) Fast Fourier transform amplitude of $[V_0(t)]^n$, indicating the bandwidth of the corresponding order in the time-dependent inversion algorithm. Dashed black line: Cutoff amplitude of 5×10^{-4} applied in Eq. (15). (b), (c) Fast Fourier transform amplitude of the simulated transient differential conductance in Fig. 8(a): 1 ps decay (b) and Fig. 8(b): 100 fs decay (c). In each panel, top black curve: -5 V, middle black curve: -3 V, bottom black curve: -1 V. The legend in panel (c) applies to both (b) and (c), where the blue, green, and red curves in each plot are the amplitude of the fast Fourier transform of the reconstructed differential conductance for the corresponding V_{pk} (see legend) and decay time. Grey vertical lines: Frequency at which the amplitude of the Fourier transform of $V_0(t)$, $[V_0(t)]^3$, and $[V_0(t)]^5$ crosses the amplitude cutoff, leading to a loss of information in the reconstructed differential conductance (ν_1 , ν_3 , and ν_5 , respectively).

within the bandwidth of $V_0(t)$ for the 1 ps decay [Fig. 9(b)] than for the 100 fs decay [Fig. 9(c)]. In other words, when the spectral weight of the simulation is concentrated in a

frequency region where all $[V_0(t)]^n$ have sufficient spectral amplitude, the algorithm achieves near perfect reconstruction. As the speed of the dynamics is increased, the spectral weight redistributes from low to high frequency [compare Fig. 9(b) to 9(c)], leading to inaccuracies in the reconstruction, especially at low V_{pk} . Still, even for dynamics far above the bandwidth of the THz voltage pulse, the algorithm recovers the majority of the spectral content for voltages at which the I - V characteristic is highly nonlinear.

V. DISCUSSION

Subcycle THz-STs is a potentially powerful tool for ultrafast nanoscience. In anticipation of the wide range of experimental studies that may be enabled, we provide some comments below on the scope of the steady-state and time-dependent inversion algorithms.

The algorithms as they are currently formulated are not compatible with a static bias voltage, V_{DC} . Specifically, the simplifications in Eqs. (5) and (11) cannot be made because cross terms arise when $V_{total} = V_{DC} + V_{THz}(t)$ is raised to a power of n . We believe this issue can be solved by redefining the polynomial that the THz voltage pulse acts on. In short, when a static bias is present without $V_{THz}(t)$, it produces a current:

$$I_{DC} = \sum_{n=1}^N A_n V_{DC}^n. \quad (17)$$

Due to lockin detection, THz-STs measures only THz-induced current, which we label I' . A new I' - V' characteristic can be defined in which the origin is shifted from $V = 0, I = 0$ to $V = V_{DC}, I = I_{DC}$. The THz voltage pulse acts on this new I' - V' curve, such that

$$I' = \sum_{m=1}^M A'_m (V')^m, \quad (18)$$

and $V' = V_{THz}(t)$. Critically, the A'_m coefficients are *different* from the A_n coefficients of the original I - V curve defined in Eq. (4). We caution that $I'(V')$ should be considered a new intrinsic characteristic of the junction sampled by the THz voltage pulse, with V_{DC} as an external control parameter, rather than a translation of the original I - V characteristic, since the differential conductance may be frequency dependent and moving the origin will mix the inaccessible linear term of the polynomial with other orders.

Another adaptation to the algorithm could be to use a different basis set for the I - V curve (i.e., not a polynomial). Other basis sets could prove well-matched to certain shapes and be employed accordingly.

The time-dependent algorithm may be further improved by optimizing how the loss of information at the cutoff amplitude is managed. We have demonstrated one option, which is to set $\mathcal{F}\{A_n\}(v)$ to zero when the amplitude of $\mathcal{F}\{[V_0]^n\}(v)$ is below threshold. Another approach, which reduces discontinuities, is to set $\mathcal{F}\{A_n\}(v)$ equal to its value just above threshold for all frequencies where $\mathcal{F}\{[V_0]^n\}(v)$ is below threshold. Regardless, any choice will involve assumptions because information is inaccessible outside of the order-dependent bandwidth.

An important future prospect is to develop an inversion algorithm for THz-pump/THz-STM-probe experiments. The steady-state and time-dependent algorithms introduced here both assume that the THz voltage pulse does not change the differential conductance. However, it has been shown experimentally that a THz voltage transient can excite sample dynamics, for example, molecular motion triggered by THz-induced tunneling [5,11,13] or by the local force of the THz field transient [11,13]. Another scenario is Coulomb blockade dynamics, where the THz-induced tunneling of one electron alters the potential energy landscape encountered by subsequent electrons. This change could occur within the oscillations of the THz voltage and depend on the waveform shape and field strength. It should be possible to identify such behavior from THz-pulse autocorrelation measurements, but an analysis algorithm beyond what is shown in this paper will be needed to disentangle it.

For the algorithms presented here, it is also important to consider the material properties that are probed. Following Ref. [23], in conventional STS the LDOS of the sample can be approximated as

$$\rho_{\text{sample}}(V) = \frac{\hbar}{4\pi^2 \rho_{\text{tip}} T(V)} \left[\frac{dI}{dV} + \frac{ed\sqrt{2m_e}}{2\hbar\sqrt{\Phi}} I(V) \right], \quad (19)$$

where ρ_{sample} is the sample LDOS, ρ_{tip} is the tip DOS, $T(V)$ is transmission probability, d is the tunnel barrier width, m_e is the electron mass, and $\Phi = (\Phi_t + \Phi_s)/2$. We note that this expression is often further approximated as $\rho_{\text{sample}} \propto dI/dV$ in the literature. The steady-state THz-STS inversion algorithm provides $I(V)$ through Eq. (8) and dI/dV through Eq. (9), with the notable exception of the Ohmic contribution to $I(V)$ and dI/dV . Yet, Eq. (19) may not hold for THz-STS. As has been shown for silicon [7], the physical response of a tip-sample junction can significantly differ for a THz voltage probe compared to a DC one, emphasizing the need for a THz-STS inversion algorithm. A reformulation of Eq. (19) may therefore be necessary for some steady-state THz-STS experiments. It will certainly be required to model pump-probe THz-STS. Optical excitation can transiently modify ρ_{sample} , ρ_{tip} , and $T(V)$ within Eq. (19), create a nonequilibrium filling of ρ_{sample} and ρ_{tip} , or stimulate more complex dynamics.

In addition to ρ_{sample} , conventional STM can also resolve surface band structure through quasiparticle interference (QPI) imaging [40,41]. Differential conductance images are recorded near a defect or step edge, showing oscillatory (interference) features. The interference can be associated with electron scattering vectors between different points of the surface band structure in the Fourier transform of the dI/dV image [41]. Repeating this procedure as a function of bias reveals cross sections of the surface band structure at different energies. The THz-STS inversion algorithm introduced here should make QPI imaging possible for THz-STM as well. A spatial map of $Q_{\text{THz}}(V_{\text{pk}})$ could be used to reconstruct the differential conductance at each tip location, and hence extract differential conductance images for each V_{pk} . Yet more excitingly, applying a similar procedure to $Q_{\text{THz}}(V_{\text{pk}}, \tau)$ should yield ultrafast QPI images of dynamics, though the experimental stability of THz-STM may need to be improved before this is feasible. Conversely, the stability

required for both of the algorithms presented in this paper has been demonstrated very recently in Ref. [42]. There, minutes-long constant-height THz-STM imaging shows that present machines are capable of acquiring datasets large enough for time-dependent THz-STS. It will, however, be a challenge to acquire a data set of the same magnitude at each pixel of a QPI image.

Although experimental THz-STS tests are beyond the scope of this paper, we have also successfully tested the steady-state algorithm using an experimental THz voltage waveform recorded by photoemission sampling (PES) [9,10,28]. However, this test assumes that the waveform measured by PES accurately describes the voltage applied across the tunnel junction. This is a key experimental question, since the accuracy of the inversion algorithm hinges on knowing the correct waveform shape. The answer may prove to be sample dependent, as local THz resonances could lead to voltage waveform shapes that depend on the tip position. The THz field enhancement is another important parameter, and has been reported to change with the microscopic tip apex [13,16]. *In situ* voltage waveform characterization may therefore be necessary in some cases. This has been demonstrated for a single-molecule switch [13], and adaptations of this approach could be adopted for other sample systems.

Another possibility is to use multimessenger detection to corroborate and complement THz-STS measurements. For example, THz-induced luminescence has been measured in conjunction with THz-STM of metal surfaces [15]. THz-STM could also be combined with near-field microscopy, though the spatial resolution of THz near-field microscopy has so far been limited to the 10–100 nm scale [1]. To overcome this limitation, we propose an experimental concept inspired by our algorithm that can be summarized in three points: (i) The bandwidth of the current pulse induced by a THz voltage transient is far larger than the input bandwidth. (ii) A transient current emits a field $E_{\text{emit}} \propto dI/dt$. (iii) The THz field scattered from the junction at frequencies well above the input bandwidth carries atomic-scale information if no other frequency broadening effects are present. Detecting these fields may be challenging, but they should directly relate to the time-dependent current across the junction and could enable atomically resolved near-field microscopy.

Finally, inversion algorithms of the type presented here may be of interest for other research fields. We stress that the algorithms only apply when the light-matter interaction is in the strong-field regime. Yet, we anticipate that they are adaptable to lightwave-driven STM at higher frequencies [10,43] for experimental parameters when this is the case. The algorithms should be similarly applicable to other experimental geometries in which strong-field coherent control of current is read out through rectified charge [44–50]. In the interest of clear communication between research fields, we note that for light coupled to a sharp tip near a surface, the geometric asymmetry is sometimes considered in terms of an asymmetric field enhancement that results in an asymmetric near-field waveform and nonzero temporal integral. Conversely, we assume here that the geometric asymmetry can be embedded in the I - V characteristic, e.g., through a reduced work function of the tip, as is commonly done in STM literature. Similarly, we treat the voltage waveform as an input rather than as a

net field (i.e., it is independent of the resulting current) so rectified charge does not affect the temporal integral of the voltage waveform either.

VI. CONCLUSIONS

In conclusion, we have introduced an algorithm to invert THz-STs data recorded in steady-state and pump-probe experiments. From an experimental perspective, the key is to record the rectified charge as a function of peak THz voltage and, in the time-dependent case, optical-pump/THz-probe delay. Polynomial fits to these data are used as the input to the algorithm. The algorithm yields the differential conductance sampled by the THz voltage pulse and achieves subcycle time resolution. By alleviating the need for guess-and-check

modeling, the algorithm advances THz-STs as a diagnostic tool for ultrafast nanoscience. Experimental tests are still needed to confirm the effectiveness of the algorithm and will, in turn, guide further algorithm refinement. In general, we expect the algorithm introduced here will serve as a launching point for subcycle THz-STs by both enabling more sophisticated experimental analysis and motivating future theoretical development.

ACKNOWLEDGMENTS

This work was supported by the Department of the Navy, Office of Naval Research (Awards No. N00014-19-1-2051, No. N00014-21-1-2682, and No. N00014-21-1-2537) and the Cowen Family Endowment.

-
- [1] T. L. Cocker, V. Jelic, R. Hillenbrand, and F. A. Hegmann, *Nat. Photon.* **15**, 558 (2021).
- [2] J. Lloyd-Hughes, P. M. Oppeneer, T. Pereira dos Santos, A. Schleife, S. Meng, M. A. Sentef, M. Ruggenthaler, A. Rubio, I. Radu, M. Murmane, X. Shi, H. Kapteyn, B. Stadtmüller, K. M. Dani, F. H. da Jornada, E. Prinz, M. Aeschlimann, R. L. Milot, M. Burdanova, J. Boland, T. L. Cocker, and F. A. Hegmann, *J. Phys.: Condens. Matter* **33**, 353001 (2021).
- [3] T. Tachizaki, K. Hayashi, Y. Kanemitsu, and H. Hirori, *APL Mater.* **9**, 060903 (2021).
- [4] T. L. Cocker, V. Jelic, M. Gupta, S. J. Molesky, J. A. J. Burgess, G. De Los Reyes, L. V. Titova, Y. Y. Tsui, M. R. Freeman, and F. A. Hegmann, *Nat. Photon.* **7**, 620 (2013).
- [5] T. L. Cocker, D. Peller, P. Yu, J. Repp, and R. Huber, *Nature (London)* **539**, 263 (2016).
- [6] K. Yoshioka, I. Katayama, Y. Minami, M. Kitajima, S. Yoshida, H. Shigekawa, and J. Takeda, *Nat. Photon.* **10**, 762 (2016).
- [7] V. Jelic, K. Iwaszczuk, P. H. Nguyen, C. Rathje, G. J. Hornig, H. M. Sharum, J. R. Hoffman, M. R. Freeman, and F. A. Hegmann, *Nat. Phys.* **13**, 591 (2017).
- [8] K. Yoshioka, I. Katayama, Y. Arashida, A. Ban, Y. Kawada, K. Konishi, H. Takahashi, and J. Takeda, *Nano Lett.* **18**, 5198 (2018).
- [9] S. Yoshida, H. Hirori, T. Tachizaki, K. Yoshioka, Y. Arashida, Z.-H. Wang, Y. Sanari, O. Takeuchi, Y. Kanemitsu, and H. Shigekawa, *ACS Photon.* **6**, 1356 (2019).
- [10] M. Müller, N. M. Sabanés, T. Kampfrath, and M. Wolf, *ACS Photon.* **7**, 2046 (2020).
- [11] D. Peller, L. Z. Kastner, T. Buchner, C. Roelcke, F. Albrecht, N. Moll, R. Huber, and J. Repp, *Nature (London)* **585**, 58 (2020).
- [12] Y. Luo, V. Jelic, G. Chen, P. H. Nguyen, Y. J. R. Liu, J. A. M. Calzada, D. J. Mildener, and F. A. Hegmann, *Phys. Rev. B* **102**, 205417 (2020).
- [13] D. Peller, C. Roelcke, L. Z. Kastner, T. Buchner, A. Neef, J. Hayes, F. Bonafé, D. Sidler, M. Ruggenthaler, A. Rubio, R. Huber, and J. Repp, *Nat. Photon.* **15**, 143 (2021).
- [14] S. Yoshida, Y. Arashida, H. Hirori, T. Tachizaki, A. Taninaka, H. Ueno, O. Takeuchi, and H. Shigekawa, *ACS Photon.* **8**, 315 (2021).
- [15] K. Kimura, Y. Morinaga, H. Imada, I. Katayama, K. Asakawa, K. Yoshioka, Y. Kim, and J. Takeda, *ACS Photon.* **8**, 982 (2021).
- [16] M. Abdo, S. Sheng, S. Rolf-Pissarczyk, L. Arnhold, J. A. J. Burgess, M. Isobe, L. Malavolti, and S. Loth, *ACS Photon.* **8**, 702 (2021).
- [17] Y. H. Kwok, G. H. Chen, and S. Mukamel, *Nano Lett.* **19**, 7006 (2019).
- [18] T. Shi, J. I. Cirac, and E. Demler, *Phys. Rev. Res.* **2**, 033379 (2020).
- [19] M. Frankerl and A. Donarini, *Phys. Rev. B* **103**, 085420 (2021).
- [20] M. Peplow, *Nature (London)* **544**, 408 (2017).
- [21] R. Wiesendanger, *Scanning Probe Microscopy and Spectroscopy* (Cambridge University Press, New York, 1994).
- [22] C. J. Chen, *Introduction to Scanning Tunneling Microscopy* 2nd edn. (Oxford University Press, New York, 2008).
- [23] B. Voigtländer, *Scanning Probe Microscopy—AFM and STM* (Springer, New York, 2015).
- [24] B. Kosłowski, C. Dietrich, A. Tschetschetkin, and P. Ziemann, *Phys. Rev. B* **75**, 035421 (2007).
- [25] B. Kosłowski, H. Pfeifer, and P. Ziemann, *Phys. Rev. B* **80**, 165419 (2009).
- [26] M. Passoni, F. Donati, A. Li Bassi, C. S. Casari, and C. E. Bottani, *Phys. Rev. B* **79**, 045404 (2009).
- [27] B. Naydenov and John J. Boland, *Phys. Rev. B* **82**, 245411 (2010).
- [28] L. Wimmer, G. Herink, D. R. Solli, S. V. Yalunin, K. E. Echternkamp, and C. Ropers, *Nat. Phys.* **10**, 432 (2014).
- [29] L. Gingras and D. G. Cooke, *Optica* **4**, 1416 (2017).
- [30] Z. Hu, Y. H. Kwok, G. H. Chen, and S. Mukamel, *Nano Lett.* **21**, 6569 (2021).
- [31] L. V. Keldysh, *Sov. Phys. JETP* **20**, 1307 (1965).
- [32] A. M. Zheltikov, *Phys. Rev. A* **94**, 043412 (2016).
- [33] J. G. Simmons, *J. Appl. Phys.* **34**, 1793 (1963)
- [34] J. G. Simmons, *J. Appl. Phys.* **34**, 238 (1962)
- [35] G. Nunes, Jr. and M. R. Freeman, *Science* **262**, 1029 (1993).
- [36] G. M. Steeves, A. Y. Elezzabi, and M. R. Freeman, *Appl. Phys. Lett.* **70**, 1909 (1997).
- [37] J. Repp, G. Meyer, S. M. Stojković, A. Gourdon, and C. Joachim, *Phys. Rev. Lett.* **94**, 026803 (2005).
- [38] A. Savitzky and M. J. E. Golay, *Anal. Chem.* **36**, 1627 (1964).
- [39] M. Eisele, T. L. Cocker, M. A. Huber, M. Plankl, L. Viti, D. Ercolani, L. Sorba, M. S. Vitiello, and R. Huber, *Nat. Photon.* **8**, 841 (2014).

- [40] K. McElroy, R. W. Simmonds, J. E. Hoffman, D. H. Lee, J. Orenstein, H. Eisaki, S. Uchida, and J. C. Davis, *Nature (London)* **422**, 592 (2003).
- [41] A. J. Macdonald, Y.-S. Tremblay-Johnston, S. Grothe, S. Chi, P. Dosanjh, S. Johnston, and S. A. Burke, *Nanotechnology* **27**, 414004 (2016).
- [42] S. E. Ammerman, V. Jelic, Y. Wei, V. N. Breslin, M. Hassan, N. Everett, S. Lee, Q. Sun, C. A. Pignedoli, P. Ruffieux, R. Fasel, and T. L. Cocker, *Nat. Commun.* **12**, 6794 (2021).
- [43] M. Garg and K. Kern, *Science* **367**, 411 (2020).
- [44] A. Schiffrin, T. Paasch-Colberg, N. Karpowicz, V. Apalkov, D. Gester, S. Mühlbrandt, M. Korbman, J. Reichert, M. Schultze, S. Holzner, J. V. Barth, R. Kienberger, R. Ernstorfer, V. S. Yakovlev, M. I. Stockman, and F. Krausz, *Nature (London)* **493**, 70 (2013).
- [45] T. Rybka, M. Ludwig, M. F. Schmalz, V. Knittel, D. Brida, and A. Leitenstorfer, *Nat. Photon.* **10**, 667 (2016).
- [46] S. Li and R. R. Jones, *Nat. Commun.* **7**, 13405 (2016).
- [47] T. Kang, R. H. J.-Y. Kim, G. Choi, J. Lee, H. Park, H. Jeon, C.-H. Park, and D.-S. Kim, *Nat. Commun.* **9**, 4914 (2018).
- [48] S. L. Lange, N. K. Noori, T. M. B. Kristensen, K. Steenberg, and P. U. Jepsen, *J. Appl. Phys.* **128**, 070901 (2020).
- [49] D. Matte, N. Chamanara, L. Gingras, Laurent P. René de Cotret, T. L. Britt, B. J. Siwick, and D. G. Cooke, *Phys. Rev. Res.* **3**, 013137 (2021).
- [50] P. Zhang, Y. S. Ang, A. L. Garner, A. Valfells, J. W. Luginsland, and L. K. Ang, *J. Appl. Phys.* **129**, 100902 (2021).